

Characterization and modeling of a low background HPGe detector

N. Dokania^{a,b}, V. Singh^{a,b}, S. Mathimalar^{a,b}, V. Nanal^{c,*}, S. Pal^c,
R.G. Pillay^c

^a*India based Neutrino Observatory, Tata Institute of Fundamental Research, Mumbai 400 005, India.*

^b*Homi Bhabha National Institute, Anushaktinagar, Mumbai 400 094, India.*

^c*Department of Nuclear and Atomic Physics, Tata Institute of Fundamental Research, Mumbai 400 005, India.*

Abstract

A high efficiency, low background counting setup has been made at TIFR consisting of a special HPGe detector ($\sim 70\%$) surrounded by a low activity copper+lead shield. Detailed measurements are performed with point and extended geometry sources to obtain a complete response of the detector. An effective model of the detector has been made with GEANT4 based Monte Carlo simulations which agrees with experimental data within 5%. This setup will be used for qualification and selection of radio-pure materials to be used in a cryogenic bolometer for the study of Neutrinoless Double Beta Decay in ^{124}Sn as well as for other rare event studies. Using this setup, radio-impurities in the rock sample from India-based Neutrino Observatory (INO) site have been estimated.

Keywords: HPGe detector, Monte Carlo Simulation

PACS: 29.30.Kv, 29.40.Wk, 02.70.Uu

¹ 1. Introduction

² Understanding and minimization of background plays a very important
³ role in rare decay studies like Double Beta Decay (DBD). For such rare

^{*}Corresponding author. Tel.: +91-22-22782333; fax: +91-22-22782133.

Email address: `nanal@tifr.res.in` (V. Nanal)

4 processes ($T_{1/2} > 10^{20}$ years), the sensitivity of measurement depends criti-
5 cally on the background level in the region of interest (ROI). The natural
6 radioactivity from the surroundings ($^{232}\text{Th} - T_{1/2} \sim 10^{10}$ years, $^{235}\text{U} - T_{1/2}$
7 $\sim 10^8$ years, $^{238}\text{U} - T_{1/2} \sim 10^9$ years, $^{40}\text{K} - T_{1/2} \sim 10^9$ years, etc.), setup ma-
8 terials and the detector itself are the source of α, β, γ and neutrons. Further,
9 muon-induced interactions in the materials surrounding the detector give rise
10 to additional background of γ -rays and neutrons. While it is impossible to
11 completely eliminate these background sources, it is essential to minimize the
12 same. The flux of cosmic ray muons can be significantly reduced in an un-
13 derground laboratory. Background from internal sources can be minimized
14 by careful selection of radio pure materials [1, 2], while the background from
15 the external sources is reduced by suitable shielding. In recent experiments,
16 ultra low levels of background $\geq 10^{-3}$ cts/(keV kg year) have been claimed
17 using special materials and novel techniques [3, 4]. The total background,
18 both from external and internal sources, has to be taken into consideration
19 during the interpretation of results. Generally, a background model employ-
20 ing Monte Carlo (MC) simulations taking into account all the contributions
21 from the actual setup and the environment in the experimental site is used
22 for physics analysis [5–8].

23 To assess the level of radio purity in the materials surrounding the detec-
24 tor, samples are often counted in a close geometry to obtain high counting
25 efficiency. For accurate determination of radio impurities, precise knowl-
26 edge of detection efficiency over a wide energy range is necessary. The effi-
27 ciency measurement in a close geometry is complicated using standard multi-
28 gamma sources due to coincidence summing effects. Hence, measurements
29 are restricted to available mono-energetic sources in a limited energy range.
30 Consequently, MC simulation technique is adopted to obtain efficiency of the
31 detector over a wide energy range for different source-detector configurations.
32 It has been observed in the literature [9–16] that the efficiency computed from
33 the MC simulations using the detector geometry supplied by the manufac-
34 turer is overestimated (by $\geq 10\%$) as compared to the experimental values.
35 The discrepancy in efficiency is attributed to the inaccuracy of the supplied
36 parameters, like detector size and the dead layer. It should be mentioned
37 that this effect is more pronounced for large size detectors [13, 14], which
38 may be due to incomplete charge collection. Thus, the parameters of the
39 detector need to be optimized by detailed measurements along the detector
40 surfaces covering the energy range of interest. In addition, measurements at
41 different distance for various source geometries are required to extract the

42 active volume.

43 A feasibility study to search for $0\nu\beta\beta$ in ^{124}Sn using a tin cryogenic
44 bolometer [17–19] has been initiated at the upcoming underground facility in
45 India-based Neutrino Observatory (INO) [20]. In case of ^{124}Sn , $Q_{\beta\beta}=2.293$
46 MeV [21] is close to the Compton edge of 2.614 MeV γ -ray, originating in
47 the decay chain of $^{232}\text{Th} (^{208}\text{Tl} \xrightarrow{\beta^-} {}^{208}\text{Pb}(3^-) \xrightarrow{\gamma} {}^{208}\text{Pb}(0^+))$. To investigate the
48 background issues pertaining to NDBD search in ^{124}Sn , a low background
49 counting setup with HPGe detector has been made at sea level in TIFR,
50 Mumbai. This setup is intended for screening of materials in the prototype
51 bolometer R&D at TIFR as well as for understanding the background. In
52 addition, the setup will be used for rare event studies like DBD to the excited
53 states of daughter nuclei, rare alpha decays etc. [22–27]. This paper describes
54 the optimization of the HPGe detector model using MC simulations. In the
55 present work, mono-energetic sources are used to scan the Ge crystal in di-
56 rections parallel and perpendicular to its cylindrical axis. Measurements are
57 also done with sources over an energy range of $E_\gamma=100\text{--}1500$ keV as a function
58 of distance to estimate its active volume. Experimental details are discussed
59 in Section 2. Section 3 describes the procedure of MC simulations as well
60 as the optimization of different parameters of the crystal, namely, the top
61 and side dead layer, front gap, radius, length and hole size. Results of the
62 detector model and measurements in the low background counting setup are
63 presented in Section 4 and conclusions are given in Section 5.

64 2. Experimental Details

65 The HPGe detector is a coaxial p-type Ge (ORTEC GEM75-95-LB-C-
66 HJ), specially designed for low background measurements with a relative
67 efficiency of $\sim 70\%$. It has a low background carbon fiber outer body and
68 copper support structures with a 60 cm long cold finger attached to a J-
69 shaped cryostat. Figure 1a shows a schematic view of the experimental setup
70 together with the inner 5 cm low activity OFHC Cu shield and the outer
71 10 cm low activity Pb shield (<0.3 Bq/kg ^{210}Pb). Figure 1b shows the cross-
72 sectional view of the detector indicating different parameters. The detector
73 bias used is +4 kV, as recommended by the manufacturer. The nominal
74 size of the Ge crystal given by the manufacturer is 78.3 mm diameter and
75 63 mm length with a 0.7 mm dead layer on the cylindrical side. In addition to
76 electrical contacts, the detector is surrounded by aluminized mylar and thin
77 copper on sides as well as on bottom for thermal shielding. Generally, the

78 physical dimensions of the detector can be determined by radiography [9, 28]
 79 but the active volume of the detector may differ depending on the electric
 80 field configuration inside the crystal [14]. Precise measurements of photopeak
 81 efficiencies using radioactive sources give better estimates on the actual active
 82 volume and the surrounding materials of the detector. In the present case,
 83 radiography of the setup was not possible and hence mono-energetic sources
 84 covering an energy range of 59.5–1115.5 keV were used to scan the crystal.
 85 Table 1 gives the details of various sources and source geometries used in the
 present work together with respective gamma ray energies.

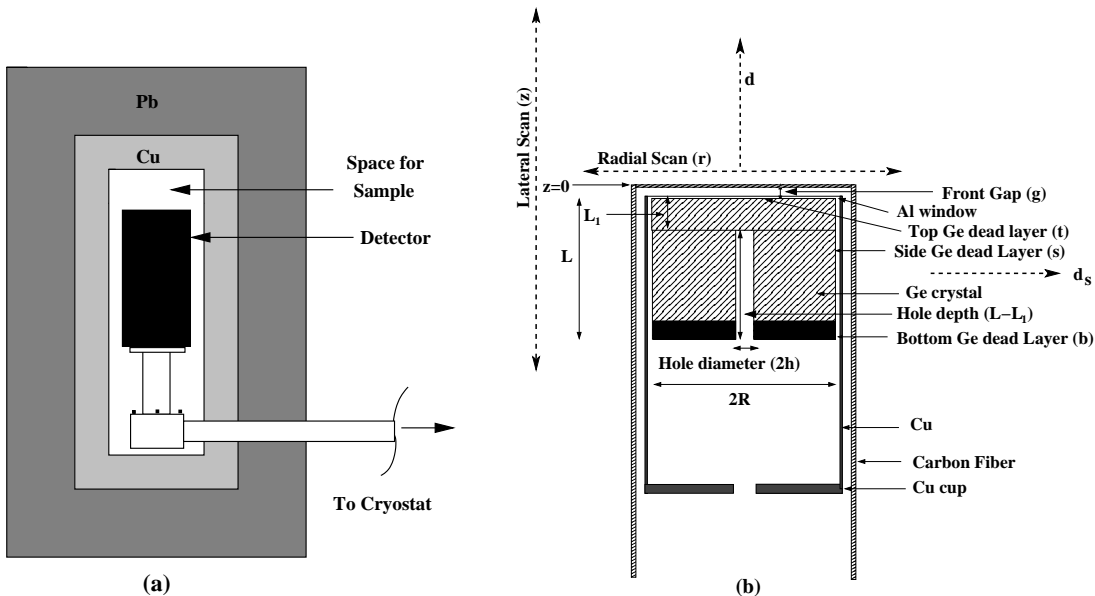


Figure 1: (a) A schematic view of low background counting setup comprising the HPGe detector, ~ 5 cm Cu shield, outer 10 cm low activity Pb shield and showing the space for sample, (b) A cross-sectional view of the detector showing different parameters. Scan directions for lateral, radial, top (d) and side (d_s) are also indicated. The center of the detector corresponds to $r=0$ and the top edge of the detector, i.e. carbon fiber housing, corresponds to $z=0$.

Table 1: List of radioactive sources used for measurements.

Isotopes	Energy (keV)	Geometry
^{241}Am	59.5	point
^{57}Co	122.1	extended
^{203}Hg	279.2	extended
^{51}Cr	320.1	extended
^{137}Cs	661.7	volume
^{54}Mn	834.8	extended
^{65}Zn	1115.5	extended
^{152}Eu	121.8, 778.9, 1408	point
^{60}Co	1173.2, 1332.5	point

87 Measured absolute strengths of sources are in the range of \sim 1-90 kBq
 88 with \sim 0.8-1.5% uncertainty. The extended geometry source has a 6 mm
 89 active diameter and is mounted on a 25 mm diameter plastic disc with a
 90 1 mm thick plastic front cover. In case of ^{137}Cs volume source, the liquid was
 91 sealed inside a perspex cylindrical vial of radius 3 mm and height 5 mm. The
 92 distribution of ^{137}Cs volume source was assumed to be homogeneous in the
 93 perspex vial. Measurements for optimizing detector geometry can be broadly
 94 classified into three categories (see Figure 1b), namely, radial scan, lateral
 95 scan and distance scan for volume effect. Radial and lateral scans are carried
 96 out with ^{241}Am , ^{57}Co and ^{65}Zn sources. The low energy gamma-rays are
 97 sensitive to the dead layers and high energy gamma-rays probe the detector
 98 size. Radial scan was done by moving the source parallel to the top detector
 99 face (r) at a distance of 5 mm in 3 mm steps and covered a range of \pm 6 cm
 100 w.r.t. the center of the detector. For the lateral scan the source was moved
 101 parallel to its cylindrical axis (z) at a distance of 8 mm from the side face
 102 of the detector in 3 mm steps and covered a range of \pm 8 cm w.r.t. the top
 103 face of the detector. The distance scan (d) was done in steps of 5 cm over a
 104 distance of 0–25 cm from the top face as well as from the cylindrical side of
 105 the detector to study the volume effect for $E_{\gamma}=834.8$ and 1115.5 keV. Typ-
 106 ical uncertainty in positioning of the source, both in horizontal and vertical
 107 direction, was less than 1 mm. Detector signal was given to a 13-bit analog-
 108 to-digital converter through a spectroscopic amplifier (shaping time : 10 μs).
 109 Data was recorded with a CAMAC-based acquisition system, LAMPS [29].

110 Dead time correction was done using a standard 10 Hz pulser. Figure 2 shows
 111 gamma-ray energy spectra with ^{57}Co and ^{65}Zn . Typical measured energy res-
 112 olution (FWHM) obtained was 0.75(2) keV at 122.1 keV and 1.84(2) keV at
 113 1115.5 keV, respectively. Photopeak efficiency (ϵ^{exp}) was extracted using
 114 LAMPS software by fitting the observed photopeak to a Gaussian function
 115 with either a linear or a quadratic background. In some cases, the observed
 116 peak had a slight low energy tail, which could be incorporated in the fit-
 117 ting software. However, the contribution from tail region was found to be
 118 negligible. In the present case, given relatively low source strengths no pile
 119 up effects have been observed in the spectra. Errors were computed includ-
 120 ing statistical errors and least-squares fitting errors in extracting the peak
 121 areas. Typical errors obtained in ϵ^{exp} were : in radial/lateral scans $\sim 3.7\%$
 122 for $E_{\gamma}=59.5$ keV, 0.2% for $E_{\gamma}=122.1$ keV and 1.8% for $E_{\gamma}=1115.5$ keV. It
 123 should be mentioned that differences in statistical errors are mainly due to
 124 the difference in strengths of various sources and energy dependent variation
 125 in detection efficiency. Similarly, for both the top and side distance scan
 126 errors in ϵ^{exp} were $\sim 2\%$ and $\sim 5\%$, respectively.

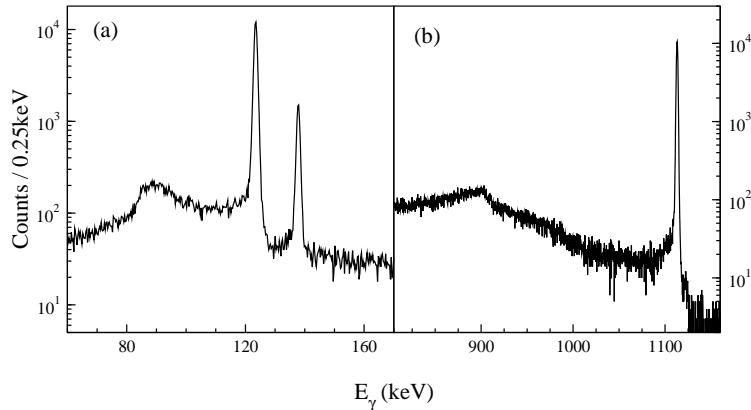


Figure 2: Gamma ray spectra obtained with (a) ^{57}Co at $d=10$ cm, and (b) ^{65}Zn source at $d=1$ cm.

127 To verify the detector model, additional radial scans with ^{57}Co and ^{65}Zn
 128 sources at $d=10.7$ cm were carried out and distance scan (~ 1 –30 cm) was
 129 done with various sources covering an energy range of 122.1–1408 keV. In this
 130 case, multi-gamma sources such as ^{152}Eu and ^{60}Co were used at a distance
 131 $d > 10$ cm to ensure that the coincidence summing is negligible. Measure-
 132 ments were also done with the volume source ($E_{\gamma}=661.7$ keV).

133 **3. Monte Carlo Simulations**

134 In the present work, GEANT4 (version 4.9.5.p01) [30] is used to simulate
 135 the HPGe detector response. The coaxial geometry of Ge crystal with a cen-
 136 tral hole is realized in the simulations by placing a circular disk of radius R
 137 and thickness L_1 on a hollow cylinder of length $L - L_1$, as shown in Figure 1b.
 138 The inner radius of the hollow cylinder is taken to be that of the hole (h)
 139 and the outer radius is R . The curvature of the edges of the cylinder/disk is
 140 neglected. Complete details of the surrounding absorbing materials such as
 141 top and side Ge dead layers, Al window, Cu cup support structures, outer
 142 carbon fiber body have been included in the Monte Carlo model. Source
 143 geometry is also taken into account in the MC simulations. It should be
 144 mentioned that the MC code is verified with other HPGe detector geome-
 145 tries [10, 15]. A photon of given energy is generated in the MC simulations.
 146 Simulations have been carried out for a set of detector parameters over a
 147 range of r and z in 6 mm steps corresponding to the measurements. Event
 148 by event data obtained from MC is binned in 0.25 keV bin size and absolute
 149 photopeak efficiency (ϵ^{MC}) is determined using the ROOT analysis frame-
 150 work [31]. In some cases where the source co-ordinates in the experiment
 151 (r_i, z_i) were different from those in the simulation (diff. ~ 1 mm), the ϵ^{MC}
 152 corresponding to r_i, z_i was obtained by interpolation. Statistical uncertain-
 153 ties are kept below 2%. For modeling the detector geometry, only absolute
 154 photopeak efficiencies of different γ -rays are taken into consideration. The
 155 best fit values of detector parameters are obtained by two methods. In the
 156 first method, χ^2 is determined for a data set like radial/lateral/distance scan
 157 (n points) corresponding to each source [32] using Eq. 1,

$$\chi^2 = \frac{1}{n-1} \sum_{i=1}^n \frac{(\epsilon_E^{exp}[r_i] - \epsilon_E^{MC}[r_i])^2}{\epsilon_E^{MC}[r_i]} \quad (1)$$

158 where, $\epsilon_E^{exp}(r_i)$ represents the measured absolute photopeak efficiency at r_i for
 159 a γ -ray of energy E_γ and $\epsilon_E^{MC}(r_i)$ is the corresponding simulated efficiency.
 160 In the second method, following the procedure as in [12, 13] to give similar
 161 weightage to ϵ_E for different energies, the total relative deviation between
 162 measured and simulated efficiencies is calculated as defined in Eq. 2,

$$\sigma_R = \frac{1}{n_2} \sum_{j=1}^{n_2} \left\{ \frac{1}{n_1} \sum_{i=1}^{n_1} \frac{|\epsilon_{E_j}^{exp}[r_i] - \epsilon_{E_j}^{MC}[r_i]|}{\epsilon_{E_j}^{MC}[r_i]} \right\} \quad (2)$$

163 where n_1 is number of points in each data set and n_2 is number of data sets
164 corresponding to different energies or scans.

165 *3.1. Optimization of detector model*

166 It is observed from the simulation data that the measured value of 66%
167 relative efficiency corresponds to an active volume of ~ 230 cm 3 , which is
168 significantly smaller ($\sim 20\%$) than the number quoted by the manufacturer
169 (292 cm 3). Further, a comparison of ϵ_E^{MC} using default detector parameters
170 with ϵ_E^{exp} for $E_\gamma=122.1$ to 1115.5 keV and $d=5$ to 25 cm, resulted in a large
171 relative deviation, $\sigma_R \sim 29.2(3)\%$. The response of the central core region of
172 the detector was probed by measurements with two collimators made from
173 a 5 cm thick lead block with a 13 mm (35 mm) diameter conical (cylindri-
174 cal) hole at the center. In both cases, a better agreement has been observed
175 between the simulations and the measured values for the restricted central
176 volume of the detector. It is therefore necessary to optimize the size of the
177 detector to reproduce the experimental data. For generating the detector
178 model, the crystal parameters varied are (see Figure 1b) : top Ge dead layer
179 (t), side Ge dead layer (s), front gap (g) i.e., the distance between the top
180 carbon fiber and the Al window, crystal radius (R), crystal length (L_1 and
181 L) and hole radius (h). External detector parameters like thicknesses of
182 carbon fiber housing, Al window and Cu cup are taken as given by the man-
183 ufacturer. Initial crystal parameters, namely, radius ($R_i=37.5$ mm), length
184 ($L_i=55$ mm), hole radius ($h_i=6.5$ mm) and front gap ($g_i=5$ mm) were ob-
185 tained by the best fit to the scan data of $E_\gamma= 1115.5$ keV at close distance,
186 where measurements are not strongly affected by the dead layers and sur-
187 rounding materials. For the front gap estimation, the fit has been restricted
188 to the central region i.e. $r=\pm 3$ cm, to minimize the effect of radial extension
189 of crystal.

190 The dead layer on the crystal attenuates the gamma rays and is best
191 estimated with low energy gamma rays. It reduces the active volume of the
192 detector [33] and may also increase with time depending on years of operation
193 [34]. As mentioned earlier, no top dead layer (t) has been specified by the
194 manufacturer while the side dead layer (s) is quoted as 0.7 mm. The uniform
195 dead layer is employed in the simulations and values of t and s are varied in
196 the range of 0–1.2 mm and 0.7–1.5 mm, respectively. It should be mentioned
197 that a 2% variation in dead layer thickness results in $\sim 2\%$ change in the
198 photopeak efficiency for $E_\gamma=59.5$ keV. The σ_R is calculated for the central
199 region of radial (lateral) scan, namely, $r=\pm 3$ cm ($z=\pm 2.5$ cm), with 59.5 keV

200 and 122.1 keV γ -ray sources mounted close to the face of the detector. The
201 best fit values of t and s extracted corresponding to a minimum σ_R are
202 $t_{opt}=1.04\pm0.02$ mm and $s_{opt}=1.27\pm0.02$ mm.

203 The germanium disc thickness L_1 was obtained by fitting the $\epsilon^{exp}(r = 0)$
204 data of $E_\gamma=320.1$ keV close to the detector top face. Since for this energy
205 halfvalue layer for germanium is ~ 5 mm, the ϵ^{MC} is expected to have better
206 sensitivity for L_1 and has a very little dependence on dead layers. The L_1
207 was varied from 7.5 mm to 12.3 mm in steps of 0.2 mm and minimum χ^2
208 was found at $L_{1-opt}=9.7\pm0.5$ mm. Considering the physical length specified
209 by the manufacturer (L_m), an inactive Ge dead layer of thickness $b=L_m - L$
210 surrounded by a 3.5 ± 0.5 mm thick cylindrical Cu ring at the bottom of the
211 crystal is included in the model. This resulted in a better reproduction of
212 the overall shape of the measured lateral scan for low energy gamma-rays.

213 For extracting R_{opt} and L_{opt} , simulations have been carried out by varying
214 R and L in fine steps of 0.25 mm and 1 mm, respectively. Figures 3 and 4
215 show ϵ^{exp} together with ϵ^{MC} for the radial and lateral scan of $E_\gamma=1115.5$ keV,
216 respectively. It is evident that R and L are not independent of each other.
217 Therefore, the best fit values of R and L are obtained by a simultaneous fit
218 to the radial and the lateral scan data for $E_\gamma=1115.5$ keV.

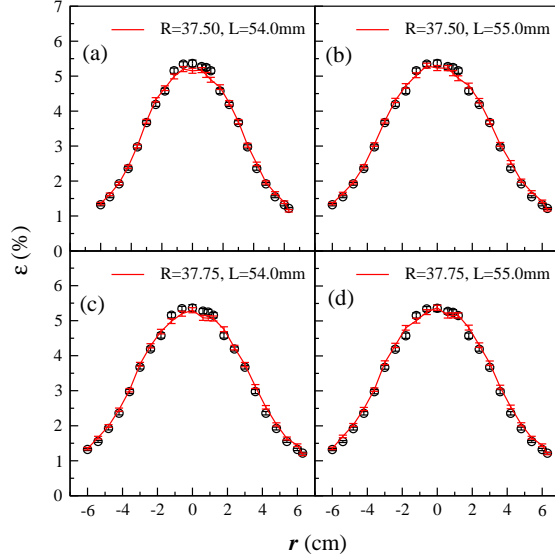


Figure 3: (Color online) The absolute photopeak efficiency ϵ^{exp} (unfilled circles) of $E_\gamma=1115.5$ keV as a function of r (radial scan). The simulated values ϵ^{MC} (lines) for different combinations of radii (R) and lengths (L) are shown in panels (a) to (d).

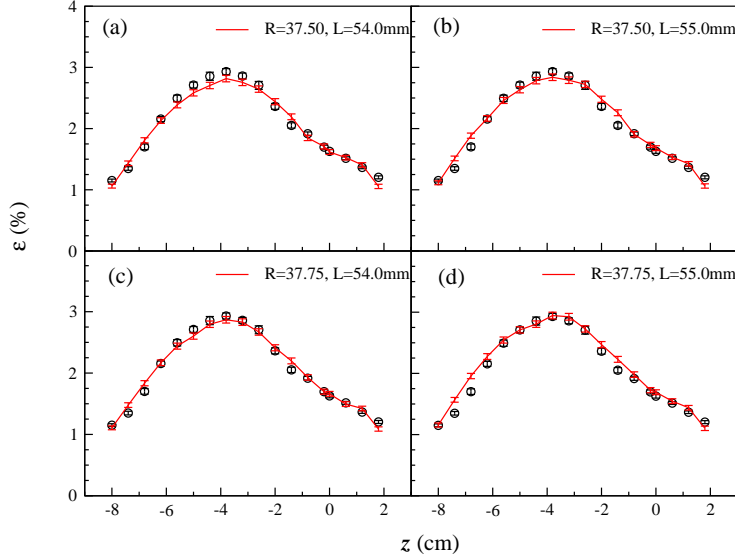


Figure 4: (Color online) The absolute photopeak efficiency ϵ^{exp} (unfilled circles) of $E_\gamma=1115.5$ keV as a function of z (lateral scan). The simulated values ϵ^{MC} (lines) for different combinations of radii (R) and lengths (L) are shown in panels (a) to (d).

219 Figure 5 shows a pictorial representation of the σ_R for radial and lateral
 220 scan. It can be seen that the minimum is rather shallow. The R_{opt} and L_{opt}
 221 are obtained from a weighted mean over the region of the shallow minimum
 222 in $R-L$ space with weight for each point taken as σ_R^{-1} . The optimal values
 223 obtained after rounding off to the first decimal place are $R_{opt}=37.6\pm0.3$ mm
 224 and $L_{opt}=54.0\pm0.9$ mm. The errors quoted are the standard deviations on
 225 the calculated quantities.

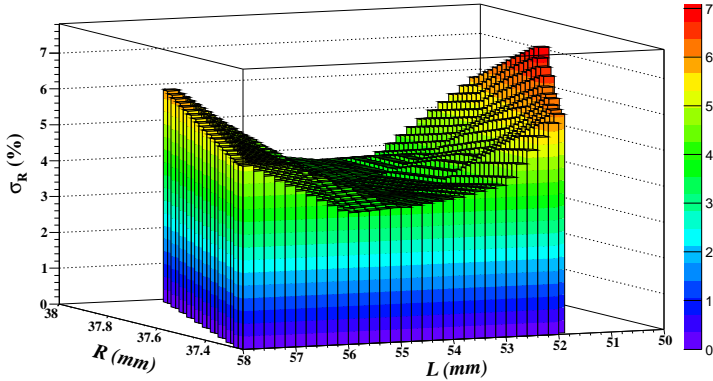


Figure 5: (Color online) The total relative deviation σ_R as a function of R and L for both radial and lateral scans with $E_\gamma=1115.5$ keV.

With above values of R_{opt} and L_{opt} , the hole depth $L_h=44.3 \pm 1.0$ mm was obtained corresponding to $L_{opt}-L_1$. The remaining unknown parameter, hole radius h , was extracted from the distance scan with high energy γ -rays. From the fit of the distance scan data (1–25 cm) of $E_\gamma= 834.8$ and 1115.5 keV, the h_{opt} was found to be 7.5 ± 0.6 mm. As mentioned earlier, the bottom dead layer b_{opt} was set to the difference between L_m and L_{opt} . Table 2 gives a complete list of optimized parameters of the detector. Errors on the parameters have been estimated from the standard deviations on the calculated quantities. The quantities marked with an asterisk in Table 2 have not been altered in the MC simulations. The nominal parameters supplied by the manufacturer are also shown for the comparison.

Table 2: Optimized parameters of the detector.

Detector Parameter	Nominal (mm)	Optimized (mm)
Ge crystal radius (R)	38.45	37.6 ± 0.3
Ge crystal total length (L)	63.0	54.0 ± 0.9
Ge disc thickness (L_1)	12.3	9.7 ± 0.5
Hole depth ($L - L_1$)	50.7	44.3 ± 1.0
Hole radius (h)	5.5	7.5 ± 0.6
Top Ge Dead Layer (t)	-	1.04 ± 0.02
Side Ge Dead Layer (s)	0.7	1.26 ± 0.02
Bottom Ge Dead Layer (b)	-	9.0 ± 1.0
Front gap (g)	4	5.0 ± 0.7
Top carbon fiber [*]	0.9	0.9
Side carbon fiber [*]	1.8	1.8
Cu Cup thickness [*]	0.8	0.8
Ge Crystal Volume (V)	292 cm^3	$232 \pm 6 \text{ cm}^3$

^{*} Not altered in MC simulations

237 4. Results

238 4.1. Validation of detector Model

239 Figures 6, 7 and 8 show a comparison of experimental data for vari-
 240 ous energies together with simulation results employing the optimized de-
 241 tector parameters. For the lateral scan with low energy gamma-rays, ad-
 242 dition of the bottom dead layer ($L_m - L_{opt} = b$) is crucial to reproduce
 243 the shape in $z=-9$ to -6 cm region (see Figures 6b and 7b). It should be
 244 mentioned that at low energy ($E_\gamma=122.1$ keV), the effective linear dimen-
 245 sion of the crystal (radius/length) seems to be lower than that for the high
 246 energy ($E_\gamma=1115.5$ keV). This could be an effect of a non-uniform electric
 247 field at corners of the crystal [14] or the non-uniform dead layer [35] or the
 248 curvature of the crystal edges (which is neglected in the simulations) [10].
 249 A comparison of data and simulation results for radial scans at $d \sim 10$ cm
 250 ($E_\gamma=122.1, 1115.5$ keV) is shown in Figure 9. Though the overall fit is good
 251 ($\sigma_R=2.8(3)\%$), the simulated spectra seems to slightly overestimate the data
 252 at higher energies (see Figure 9). For both the close geometry and distance
 253 scans, an excellent agreement is observed between simulations and data. It
 254 should be mentioned that the cylindrical symmetry of the crystal was verified

255 with $E_\gamma=59.5$ keV by placing the source in all four perpendicular directions
256 close to the detector face.

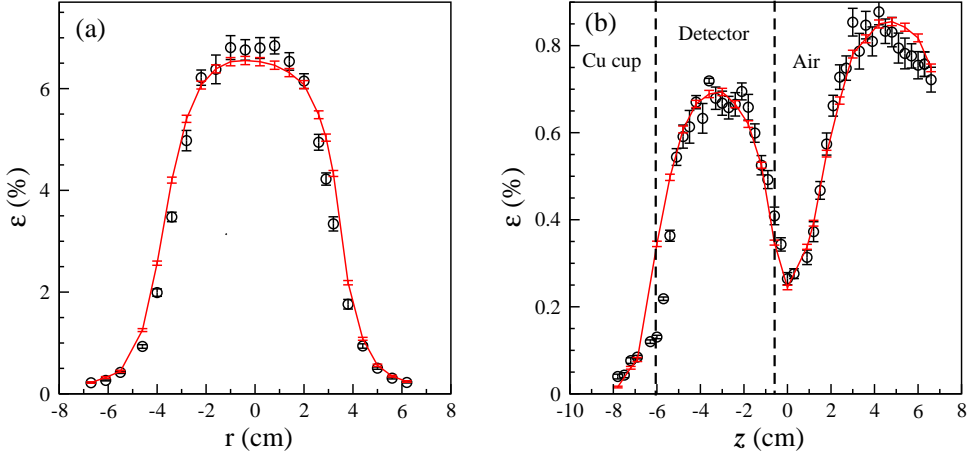


Figure 6: (Color online) The radial (left panel) and lateral (right panel) scan data of $E_\gamma=59.5$ keV with optimized detector parameters. Symbols represent the ϵ^{exp} and the line corresponds to ϵ^{MC} . The z range occupied by the crystal is marked in the figure.

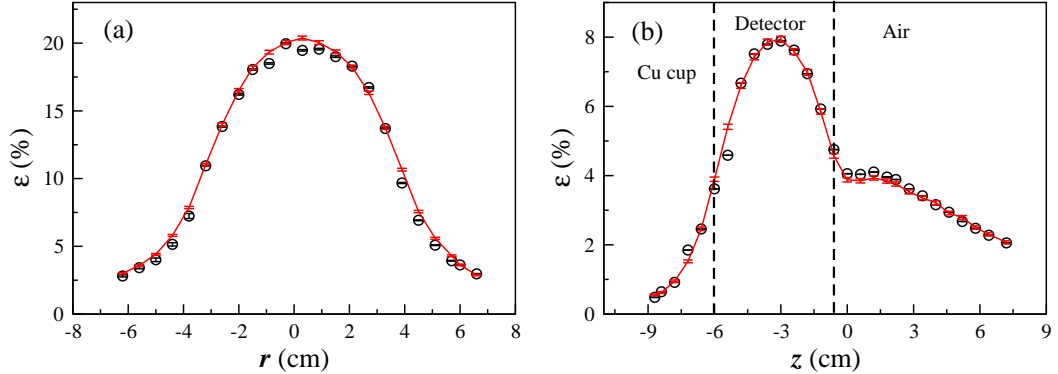


Figure 7: (Color online) Same as Figure 6 for $E_\gamma=122.1$ keV

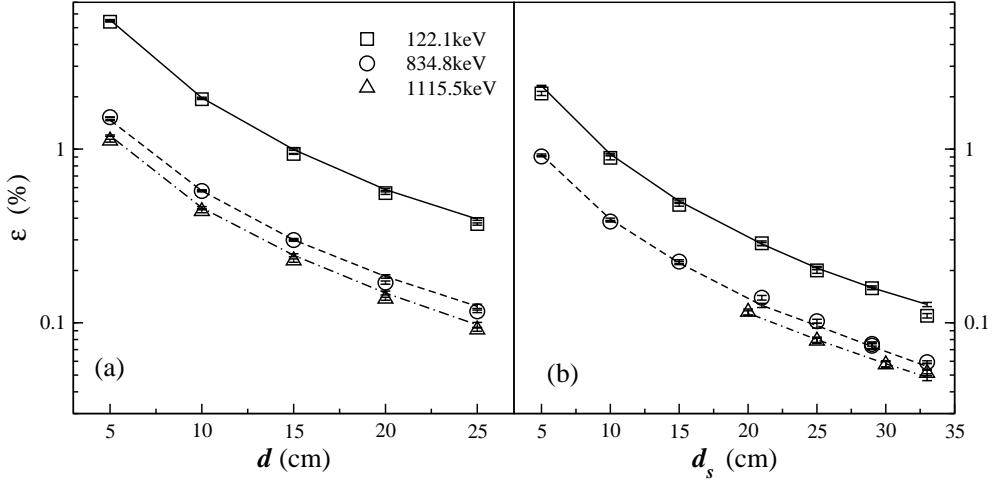


Figure 8: The top distance (left panel) and side distance (right panel) scan data of $E_\gamma=122.1, 834.8$ and 1115.5 keV with optimized detector parameters. Symbols represent the ϵ^{exp} and the line corresponds to ϵ^{MC} .

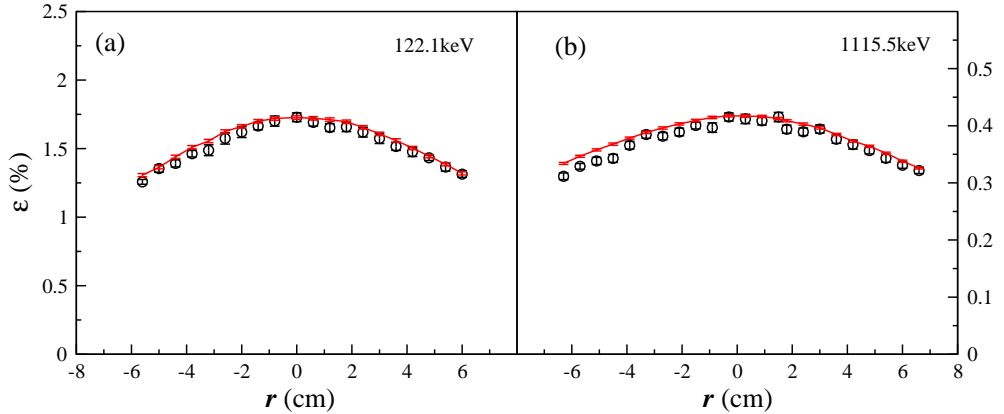


Figure 9: (Color online) The radial scans data showing ϵ^{exp} (unfilled circles) and ϵ^{MC} (lines) for (a) $E_\gamma=122.1$ keV and (b) $E_\gamma=1115.5$ keV with optimized detector parameters at $d=10.7$ cm.

257 The detector model is further tested with distance scan measurements
 258 with many sources, $E_\gamma=59.5, 279.2, 1173.2$ and 1408 keV, and results are
 259 shown in Figure 10. It is evident from both these figures that the simulations
 260 are well able to reproduce the experimental data. The effective detector

261 model was used to simulate the volume source geometry ($E_\gamma=661.7$ keV)
 262 and results are also plotted in Figure 10. The excellent agreement between
 263 measured and simulated values indicate that the optimized model works very
 264 well for different source geometries. Figure 11 displays the relative deviation
 265 σ_R for $E_\gamma=122.1, 279.2, 834.8, 1115.5$ keV as a function of $d=5-25$ cm. It
 266 can be seen that the optimized model yields $\sigma_R = 5.46(3)\%$ as opposed to
 267 $29.2(3)\%$ obtained with nominal parameters. With inclusion of low energy
 268 data of $E_\gamma=59.5$ keV, the σ_R worsens to $\sim 8.37(4)\%$.

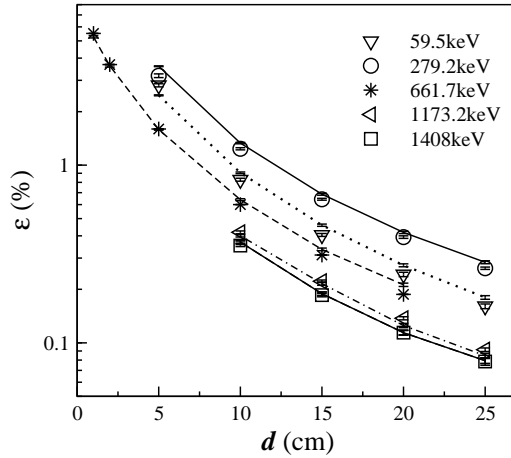


Figure 10: The ϵ^{exp} as a function of d , distance from the top face of the detector, for different gamma ray energies. Symbols represent the measured data and corresponding ϵ^{MC} with optimized parameters is shown by lines.

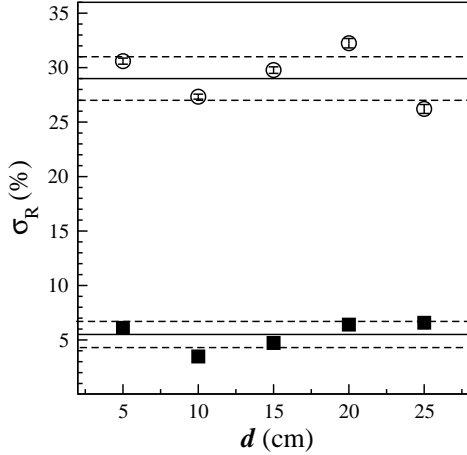


Figure 11: The relative deviation σ_R for $E_\gamma=122.1, 279.2, 834.8, 1115.5$ keV for $d=5-25$ cm obtained with optimized detector parameters (filled symbols) and with nominal parameters (open symbols). The bold line is the average and the RMS deviation is indicated by dashed lines. Errors are within the point size.

269 The measured energy spectra for ^{54}Mn source ($E_\gamma=834.8$ keV) at $d_s=25$
 270 cm and ^{137}Cs source ($E_\gamma=661.7$ keV) at $d=15$ cm is shown in Figure 12
 271 together with the simulated spectrum after folding in energy resolution of the
 272 detector. The room background has been added to the simulated spectrum
 273 for comparison with experimental spectrum. Even though the detector model
 274 was optimized with photopeak efficiency, overall spectral shape including the
 275 Compton edge, is very well reproduced. However, a slight low energy tail in
 276 the experimental spectrum ($\sim 1.5\%$) as compared to MC simulations is visible
 277 (see Figure 12). It should be mentioned that the detector has undergone two
 278 thermal cycles and an evacuation during three years of operation without
 279 any change in the performance (efficiency and resolution).

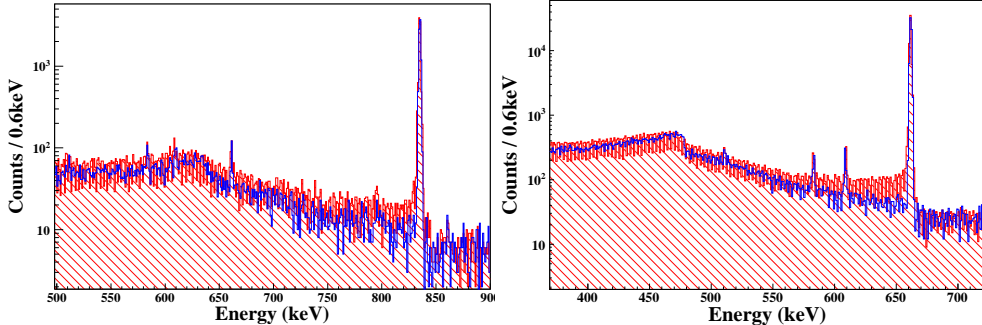


Figure 12: (Color online) The measured energy spectra (filled red) for ^{54}Mn extended source ($E_{\gamma}=834.8$ keV) at $d_s=25$ cm (left panel) and ^{137}Cs volume source ($E_{\gamma}=661.7$ keV) at $d=15$ cm (right panel) together with the simulated spectra (blue) after folding in energy resolution of the detector. The room background has been added to the simulated spectrum for comparison.

280 *4.2. Low background measurements*

281 As mentioned in the beginning, the low background counting setup is de-
 282 signed for screening materials for cryogenic bolometer. These measurements
 283 are usually of long duration (several days) and stability is very important.
 284 The gain stability of the system is monitored and drifts are found to be neg-
 285 ligibly small (\sim sub-keV) over a period of several days. With a 10 cm thick
 286 low activity Pb shield on all sides of the HPGe detector, the background
 287 gamma-rays such as $E_{\gamma}=1460.8$ keV (^{40}K) and 2614.5 keV (^{208}Tl) have been
 288 reduced by a factor of $\sim 800(60)$ and $\sim 200(19)$, respectively. The measured
 289 background level of ^{40}K is 51(7) and 166(17) counts per day with and with-
 290 out copper, respectively. Similarly for ^{208}Tl , 14(2) and 109(14) counts per
 291 day are measured in this setup with and without copper, respectively. The
 292 background levels can be further improved by addition of cosmic veto and
 293 nitrogen flushing.

294 The setup has been extensively used to test radio-impurities in various
 295 samples like the ETP copper from the Tin bolometer cryostat, ^{nat}Sn , ^{124}Sn
 296 and sensors etc. The maximum sample size that can be mounted at $d\sim 1$ cm
 297 is $9\text{ cm} \times 9\text{ cm} \times 5\text{ cm}$. The sensitivity of the setup estimated from a
 298 sample of copper used in the bolometer setup is about $\sim 1\text{mBq/g}$ for ^{232}Th
 299 and $\sim 2\text{mBq/g}$ for ^{40}K . Using this setup, the trace impurity of ^{59}Co was
 300 estimated to be 1.3(2) ppb in neutron activated Ge sample [36]. In addition,

301 the rock samples from the INO site (Bodi West Hills (BWH)) [37], the glass
 302 for RPC in ICAL detector [38] have also been studied. Figure 13 shows a
 303 spectrum of the rock sample in a close geometry together with the background
 304 spectrum, clearly indicating higher ^{40}K content in the sample. Table 3 shows
 305 estimated concentration of impurities for this sample (~ 23 g).

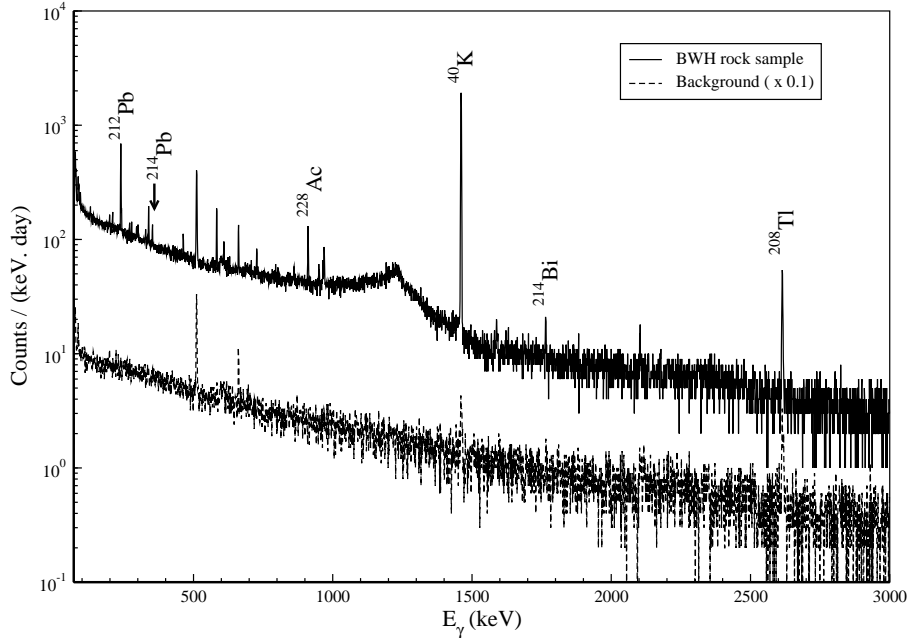


Figure 13: A gamma-ray energy spectrum (bold line) of the rock sample from the INO site (from Bodi West Hills) in the low background setup (only with Pb shield) in a close geometry. The scaled background (dashed line) without the sample is also shown for comparison.

Table 3: Estimated radio-impurity concentrations (N_x) in the BWH rock sample from the INO site using low background spectroscopy.

Element	N_x (mBq/g)
^{212}Pb	11.1(4)
^{214}Pb	1.7(4)
^{228}Ac	10.3(7)
^{40}K	1050(16)
^{208}Tl	1.8(8)
^{214}Bi	7(1)

306 It is proposed to study rare events like double beta decay to excited
 307 states using this setup, where the efficiency for required source geometry
 308 and energy range can be obtained using MC simulation technique with the
 309 effective detector model.

310 **5. Conclusions**

311 A low background counting setup has been made at TIFR consisting of
 312 a special HPGe detector surrounded by a low activity copper (5 cm)+lead
 313 (10 cm) shield. Detailed measurements are performed with point and ex-
 314 tended geometry sources to generate an effective model of the detector with
 315 GEANT4 based Monte Carlo simulations. The active volume obtained is
 316 about 20% smaller than the nominal value supplied by the manufacturer.
 317 The effective detector model agrees within 5.46(3)% with experimental data
 318 over a wide energy range of 100–1500 keV. Using the simulated efficiencies,
 319 impurities at ppb level in various samples have been measured. This low
 320 background counting setup will be used for qualification and selection of
 321 radio-pure materials to be used in the prototype bolometer R&D and for
 322 rare event studies.

323 **6. Acknowledgements**

324 The authors would like to thank Mr. M.S. Pose and Mr. K.V. Divekar for
 325 help during the setup.

326 **References**

327 [1] D.S. Leonard *et. al.*, Nucl. Instr. and Meth. A **591** (2008) 490.

328 [2] R. Arnold *et. al.*, Nucl. Instr. and Meth. A **354** (1995) 338.

329 [3] M. Agostini *et. al.*, Phys. Rev. Lett. **111** (2013) 122503.

330 [4] M. Auger *et. al.*, Phys. Rev. Lett. **109** (2012) 032505.

331 [5] M. Agostini *et. al.*, arXiv:1306.5084.

332 [6] F. Bellini, C. Bucci, S. Capelli, O. Cremonesi, L. Gironi, M. Martinez,
333 M. Pavan, C. Tomei , M. Vignati, Astroparticle Physics **33** (2010) 169.

334 [7] E. Andreotti *et al.*, Astroparticle Physics **34** (2010) 18.

335 [8] J. Argyriades *et. al.*, Nucl. Instr. and Meth. A **606** (2009) 449.

336 [9] D. Budjas, M. Heisel, W. Maneschg, H. Simgen, Appl. Radiat. and Isot.
337 **67** (2009) 706.

338 [10] Fatima Padilla Cabal, Neivy Lopez-Pino, Jose Luis Bernal-Castillo,
339 Yisel Martinez-Palenzuela, Jimmy Aguilar-Mena, Katia D'Alessandro,
340 Yuniesky Arbelo, Yasser Corrales, Oscar Diaz, Appl. Radiat. and Isot.
341 **68** (2010) 2403.

342 [11] N. Cornejo Diaz, M. Jurado Vargas, Nucl. Instr. and Meth. A **586** (2008)
343 204.

344 [12] J.C. Hardy, V.E. Iacob, M. Sanchez-Vega, R.T. Effinger, P. Lipnik,
345 V.E. Mayes, D.K. Willis, R.G. Helmer, Appl. Radiat. and Isot. **56** (2002)
346 65.

347 [13] R.G. Helmer, J.C. Hardy, V.E. Iacob, M. Sanchez-Vega, R.G. Neilson,
348 J. Nelson, Nucl. Instr. and Meth. A **511** (2003) 360.

349 [14] F. Hernandez, F. El-Daoushy, Nucl. Instr. and Meth. A **498** (2003) 340.

350 [15] S. Hurtado, M. Garcia-Leon, R. Garcia-Tenorio, Nucl. Instr. and Meth.
351 A **518** (2004) 764.

352 [16] D. Karamanis, Nucl. Instr. and Meth. A **505** (2003) 282.

353 [17] P.K. Raina *et. al.*, Ed. V.K.B. Kota and U. Sarkar, Narosa Publishers
354 (2007).

355 [18] V. Nanal, International Nuclear Physics Conference: 2013, EPJ Web of
356 Conferences (*in press*).

357 [19] V. Singh, S. Mathimalar, N. Dokania, V. Nanal, R.G. Pillay, S. Ramakr-
358 ishnan, **Pramana** **81** (2013) 719.

359 [20] N.K. Mondal, **Pramana** **79** (2012) 1003.

360 [21] D.A. Nesterenko *et. al.*, **Phys. Rev. C** **86** (2012) 044313.

361 [22] A.S. Barabash, Ph. Hubert, A. Nachab, S.I. Konovalov, I.A. Vanyushin,
362 V. Umatov, **Nucl. Phys. A** **807** (2008) 269.

363 [23] P. Belli *et. al.*, **Phys. Rev. C** **83** (2011) 034603.

364 [24] P. Belli *et. al.*, **Nuclear Physics A** **846** (2010) 143.

365 [25] P. Belli *et. al.*, **Nuclear Physics A** **859** (2011) 126.

366 [26] A. Barabash *et. al.*, **AIP Conf. Proc.** **1417** (2011) 28.

367 [27] P. Belli *et. al.*, **Phys. Rev. C** **87** (2013) 034607.

368 [28] Jonas Boson, Goran Agren, Lennart Johansson, **Nucl. Instr. and Meth.**
369 **A** **587** (2008) 304.

370 [29] <http://www.tifr.res.in/~pell/lamps.html>

371 [30] S. Agostinelli *et. al.*, **Nucl. Instr. and Meth. A** **506** (2003) 250.

372 [31] Rene Brun, Fons Rademakers, **Nucl. Instr. and Meth. A** **389** (1997) 81.

373 [32] G.F. Knoll, **Radiation Detection and Measurement**, third ed., Wiley,
374 New York, (2000).

375 [33] J. Rodenas, A. Pascual, I. Zarza, V. Serradell, J. Ortiz, L. Ballesteros,
376 **Nucl. Instr. and Meth. A** **496** (2003) 390.

377 [34] N.Q. Huy, D.Q. Binh, V.X. An, **Nucl. Instr. and Meth. A** **573** (2007)
378 384.

379 [35] D. Karamanis, V. Lacoste, S. Andriamonje, G. Barreau, M. Petit, Nucl.
380 Instr. and Meth. A **487** (2002) 477.

381 [36] N. Dokania *et. al.*, DAE Symp. on Nucl. Phys. **56** (2011) 1136.

382 [37] N. Dokania *et. al.*, DAE Symp. on Nucl. Phys. **56** (2011) 1138.

383 [38] V.M. Datar, Satyajit Jena, S.D. Kalmani, N.K. Mondal, P. Nagaraj,
384 L.V. Reddy, M. Saraf, B. Satyanarayana, R.R. Shinde, P. Verma, Nucl.
385 Instr. and Meth. A **602** (2009) 744.